Supporting Information

Lee et al. 10.1073/pnas.1801298115

SI Materials and Methods

Cloning and Protein Purification. The cloning of *P. aeruginosa slt* gene (locus tag PA3020; N-terminal signal peptide removed, Δ1–24 aa), its expression, and purification of Slt were reported previously (1). Briefly, the gene was prepared by Genscript in a pUC57 vector with NdeI and XhoI restriction sites flanking the forward and reverse end of the gene, respectively. The gene sequence was optimized for *E. coli* expression. The synthetic gene was digested by restriction enzymes NdeI and XhoI and ligated into the multiple cloning site of a pET28a(+) vector. The *P. aeruginosa* Slt catalytic mutant (E503Q) was prepared by PCR of the optimized Slt gene in the pET28a(+) vector serving as the template with primers PA3020_E503Q_Fwd 5′-catcacccggcagcaaagcgcgttcatgt-3′ and PA3020_E503Q_Rev 5′-acatgaacgcgctttgctgccgggtgatg-3′. Slt E503Q was purified as a His-tagged (N-terminal MGSSHHHHHHSSGLVPRGSHM sequence) soluble protein by Ni-NTA affinity chromatography. The His-tag of the protein was removed by thrombin per the manufacturer's instruction (Sigma). Thrombin cleavage proceeded for 18 h at 4 °C, and the resulting protein encoded a remaining N-terminal GSHM sequence. SDS/PAGE analysis showed that the purity of Slt and Slt catalytic mutant (E503Q) (before and after removal of His-tag) exceeded 95%.

Analysis of Enzymatic Activities of Wild-Type Slt and E503Q Slt by the Fluorescein-Labeled Sacculus Assay. The enzyme activity was monitored by an EnzChek Lysozyme Assay Kit (Thermo Fisher Scientific). The assay contains fluorescein-labeled *Micrococcus luteus* sacculus, which has been used previously as substrate for analysis of lytic transglycosylase activity. The analysis of the relative activities of the wild-type enzyme and the catalytic mutant were performed in 50 mM Na_2HPO_4 (pH 7.8) at room temperature using a Cary Eclipse Fluorescent Spectrophotometer. A single reading (excitation, 485 nm; emission, 516 nm; average scan time, 0.25 s) was collected at 1-min time intervals for 30 min, and each experiment was performed in triplicate. No evidence of photobleaching was detected. The catalytic activity of the Slt mutant E503Q was ∼0.01% of that of the wild-type enzyme.

Reaction of Slt with Synthetic Peptidoglycan. The enzymatic reactions of Slt with various synthetic substrates were carried out in 20 mM Hepes, 0.1 M NaCl, 0.1% Triton X, pH 7.0, at 23 °C, and were stopped by the addition of trifluoroacetic acid. The reaction mixture was analyzed by LC/MS. The LC/MS conditions were reported previously (2). A total of seven synthetic peptidoglycan substrates (**1**, **2**, **3**, **1p**, **2p**, **3p**, and **4p**) were used in this study, and they were prepared by the methodologies reported previously (1–5). The reactions of E503Q Slt and Slt70 (*E. coli*) (6) were carried out under the same conditions described above for Slt. Reactions are summarized in Fig. 2 and Figs. S1 and S2.

Crystallization. The wild-type Slt was used at 6 mg/mL in 50 mM Tris, 400 mM NaCl, pH 8. Crystals grew in a precipitant solution containing 1.4 M sodium potassium phosphate at pH 6.5, using the sitting drop vapor diffusion method at 291 K. For the sitting-drop vapor diffusion method, drops were prepared mixing 1 μL of protein with 1 μL of precipitant solution. Drops were equilibrated against 150 μL of precipitant in the reservoir chamber. The resulting crystals were cryoprotected with a solution containing the crystallization condition and 50% lithium phosphate, before flash cooling at 100 K.

The complex of the wild-type Slt with the reaction product (compound **IIpa**) was obtained by soaking native protein crystals in a solution containing 1.4 M sodium potassium phosphate at pH 6.5 and 5 mM compound **1p** for 12 h. These crystals were cryoprotected in the same manner as native crystals.

The Slt E503Q mutant was prepared at the same concentration and in the same buffer as the wild-type Slt. Slt E503Q crystals grew in a different condition, in 80 mM Tris, pH 8.5, 12% PEG 8000, 160 mM calcium acetate, and 8 mM CHAPS detergent, using the sitting-drop vapor diffusion method at 291 K. Inactive mutant crystals were cryoprotected with a solution containing the crystallization condition and 20% glycerol, before flash cooling at 100 K.

The complexes of Slt E503Q with the tetrasaccharides **1p** and **2p** were obtained by soaking mutant Slt E503Q crystals in a solution containing the crystallization condition and 5 mM of the specific compound for 6 h. The complex of Slt E503Q with the octasaccharide **3p** was obtained by soaking Slt E503Q crystals in a solution containing the crystallization condition and 4 mM compound **3p** for 6 h. Finally, the complex between Slt E503Q and bulgecin A was obtained by soaking crystals in a solution containing the crystallization condition and 7 mM bulgecin A for 6 h. All of these crystals were cryoprotected with a solution containing the crystallization condition and 20% glycerol, before flash cooling at 100 K.

Data Collection, Processing, and Structural Determination. All of the datasets were processed and scaled using XDS (7), iMOSFLM (8), and AIMLESS (9). The native Slt datasets were collected on beamline ID23-1 at European Synchrotron Radiation Facility using a Pilatus 6M-F detector and a wavelength of 1.0000 Å at 2.20-Å resolution. Crystals of apo Slt belong to the hexagonal space group $P6_3$ with unit cell dimensions of $a = b = 163.98$ Å and $c = 56.71$ Å, with a single molecule in the asymmetric unit (AU). Molecular replacement with Slt70 from *E. coli* (PDB ID code 1QSA) fails in phasing. In retrospect, this was not surprising in view of the large rmsd of 4.6 Å between both flexible structures. The Slt structure was solved with ARCIMBOLDO_SHREDDER (10) extracting polyalanine spherical models ranging from 42 to 177 residues, placing them with PHASER (11) and combining 12 very partial, consistent solutions in reciprocal space with ALIXE (12) before expansion. Density modification and autotracing with SHELXE (13) provided a nearly complete main-chain structure. This solution was completed by manual modeling using COOT (14), and refinement with PHENIX (15).

Datasets for inactive mutant Slt E503Q and complexes Slt:**IIpa,** Slt:**1p**, Slt:**2p**, Slt:**3p**, and Slt:bulgecin A were all collected at beamline XALOC of the ALBA synchrotron using a Pilatus 6M detector. Slt E503Q X-ray diffraction dataset were collected with wavelength of 0.97953 Å at 3.05-Å resolution. Crystals belong to $P6_3$ space group with cell dimensions of $a = b = 163.48$ Å and $c = 56.04$ Å, and with one molecule in the AU. The Slt:**1p** complex dataset was collected with wavelength of 0.97926 Å at 2.90-Å resolution. Crystals belong to $P6_3$ space group with cell dimensions of $a = b = 166.87$ Å and $c = 54.51$ Å, and with one molecule in the AU. The datasets for the complex Slt:**IIpa** were collected with wavelength of 0.97919 Å at 2.50-Å resolution. Crystals belong to $P6_3$ space group with cell dimensions of $a = b = 165.52$ Å and $c = 54.73$ Å, and with one molecule in the AU. The Slt:**2p** complex dataset was collected with wavelength of 0.97926 Å at 2.75-Å resolution. Crystals of Slt:**2p** complex belong to $P6_3$ space group with cell dimensions of $a = b = 166.70$ Å and $c = 55.34$ Å, and with one molecule in the AU. The Slt:**3p** complex X-ray

diffraction datasets were collected with wavelength of 0.97953 Å at 3.20-Å resolution. Crystals belong to $P6_3$ space group with cell dimensions of $a = b = 164.29$ Å and $c = 55.95$ Å, and with one molecule in the AU. The Slt:bulgecin A complex X-ray diffraction dataset were collected with wavelength of 0.97953 Å at 3.10-Å resolution. Crystals belong to $P6_3$ space group with cell dimensions of $a = b = 165.71$ Å and $c = 55.88$ Å, and with one molecule in the AU.

The structures of the inactive mutant Slt E503Q and the complexes were solved by the molecular replacement method using the coordinates of our Slt wild-type structure as the search model. The rotational and translational searches were performed using PHASER (16) followed by manual modeling using COOT (14) and refining with PHENIX (15). All of the statistics for data processing and refinement are shown in Table S1.

Computational Method. The crystal structure coordinates were processed for modeling using protein preparation wizard module of Schrödinger Suite (version 2015; Schrödinger, Inc.) before the computational simulations. During the preparation, hydrogen atoms were added and bond orders were assigned. Residues C130 and C163 were covalently attached to each other by a disulfide bond. The E503Q mutant was computationally modeled to the wild-type glutamic acid. The X-ray complexes guided us in modeling a peptidoglycan fragment in the Slt active site. Partial charges for the peptidoglycan atoms were calculated quantum mechanically at HF/6-31G(d) level of theory with Gaussian program (version g09; Gaussian, Inc.; 2016). Subsequently, charges were fit with RESP methodology (17), using antechamber program of AMBER16 (18). The complex was immersed in water molecules (TIP3P model) in a rectangular box with dimensions such that the protein atoms were at least 15 Å away from any of the box edges. The system was energy-minimized, equilibrated, and subjected to molecular-dynamics simulation with PMEMD module of AMBER16 program (18), applying previously reported protocol (19). To relax the modeled peptidoglycan, the initial 100-ps duration of the equilibration allowed the sugar and peptide atoms to move freely alongside water molecules, while protein coordinates were restrained with a weak force constant of 1.0 $kcal{\cdot}mol^{-1}{\cdot}Å^{-1}$. The restraints were gradually released for the solute in subsequent equilibration steps. A final production run simulation of 200 ns was performed without any restraints.

Movies S1 and S2. Morph animation of the conformational motion as demonstrated by the X-ray structures. The motion was morphed from the apo X-ray structure toward the Slt:**3p** complex. Movie S1 shows the reorganization of the active site for endolytic reaction. Movie S2 demonstrates the motion experienced by the entire protein. Animations were rendered in VMD program (20).

1. Lee M, et al. (2017) From genome to proteome to elucidation of reactions for all eleven known lytic transglycosylases from *Pseudomonas aeruginosa*. *Angew Chem Int Ed Engl* 56:2735–2739.
2. Lee M, et al. (2017) Deciphering the nature of enzymatic modifications of bacterial cell walls. *Chembiochem* 18:1696–1702.
3. Hesek D, Lee M, Morio K, Mobashery S (2004) Synthesis of a fragment of bacterial cell wall. *J Org Chem* 69:2137–2146.
4. Lee M, et al. (2010) Synthetic peptidoglycan motifs for germination of bacterial spores. *Chembiochem* 11:2525–2529.
5. Martínez-Caballero S, et al. (2013) Reaction products and the X-ray structure of AmpDh2, a virulence determinant of *Pseudomonas aeruginosa*. *J Am Chem Soc* 135:10318–10321.
6. Lee M, et al. (2013) Reactions of all *Escherichia coli* lytic transglycosylases with bacterial cell wall. *J Am Chem Soc* 135:3311–3314.
7. Kabsch W (2010) XDS. *Acta Crystallogr D Biol Crystallogr* 66:125–132.
8. Battye TGG, Kontogiannis L, Johnson O, Powell HR, Leslie AG (2011) iMOSFLM: A new graphical interface for diffraction-image processing with MOSFLM. *Acta Crystallogr D Biol Crystallogr* 67:271–281.
9. Evans PR, Murshudov GN (2013) How good are my data and what is the resolution? *Acta Crystallogr D Biol Crystallogr* 69:1204–1214.
10. Millán C, Sammito M, Usón I (2015) Macromolecular ab initio phasing enforcing secondary and tertiary structure. *IUCrJ* 2:95–105.
11. Read RJ, McCoy AJ (2016) A log-likelihood-gain intensity target for crystallographic phasing that accounts for experimental error. *Acta Crystallogr D Struct Biol* 72: 375–387.
12. Millán C, et al. (2015) Combining phase information in reciprocal space for molecular replacement with partial models. *Acta Crystallogr D Biol Crystallogr* 71:1931–1945.
13. Thorn A, Sheldrick GM (2013) Extending molecular-replacement solutions with SHELXE. *Acta Crystallogr D Biol Crystallogr* 69:2251–2256.
14. Emsley P, Lohkamp B, Scott WG, Cowtan K (2010) Features and development of Coot. *Acta Crystallogr D Biol Crystallogr* 66:486–501.
15. Afonine PV, et al. (2012) Towards automated crystallographic structure refinement with phenix.refine. *Acta Crystallogr D Biol Crystallogr* 68:352–367.
16. McCoy AJ, et al. (2007) Phaser crystallographic software. *J Appl Cryst* 40:658–674.
17. Cornell WD, Cieplak P, Bayly CI, Kollman PA (1993) Application of Resp charges to calculate conformational energies, hydrogen-bond energies, and free-energies of solvation. *J Am Chem Soc* 115:9620–9631.
18. Case DA, et al. (2017) AMBER16 (University of California, San Francisco), Version 16.
19. Mahasenan KV, et al. (2017) Conformational dynamics in penicillin-binding protein 2a of methicillin-resistant *Staphylococcus aureus*, allosteric communication network and enablement of catalysis. *J Am Chem Soc* 139:2102–2110.
20. Humphrey W, Dalke A, Schulten K (1996) VMD: Visual molecular dynamics. *J Mol Graph* 14:33–38, 27–28.

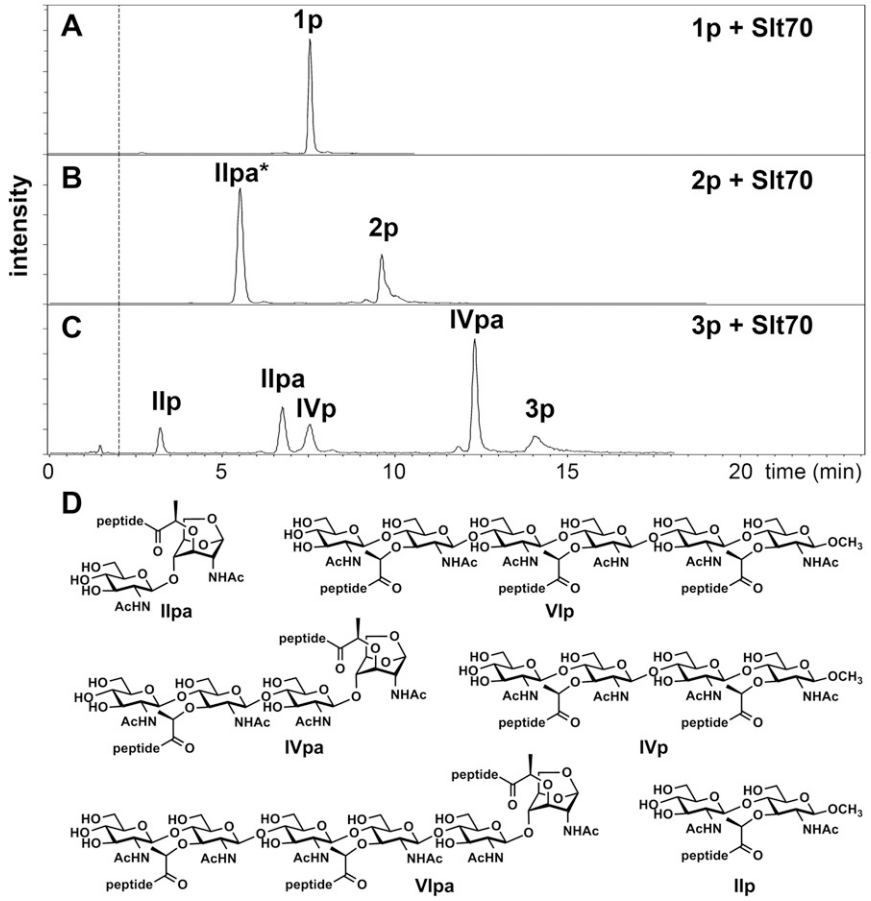

Fig. S1. Turnover of synthetic peptidoglycans by Slt70 (*E. coli*). (*A*–*C*) LC/MS traces of turnover of **1p**, **2p**, and **3p** catalyzed by Slt70. **2p** and **IIpa*** have tetrapeptide stem(s) instead of pentapeptide stem(s). (*D*) The chemical structures of turnover products of **3p**. Pentapeptide, L-Ala-γ-D-Glu-*m*-DAP-D-Ala-D-Ala (DAP for diaminopimelate); tetrapeptide, L-Ala-γ-D-Glu-*m*-DAP-D-Ala.

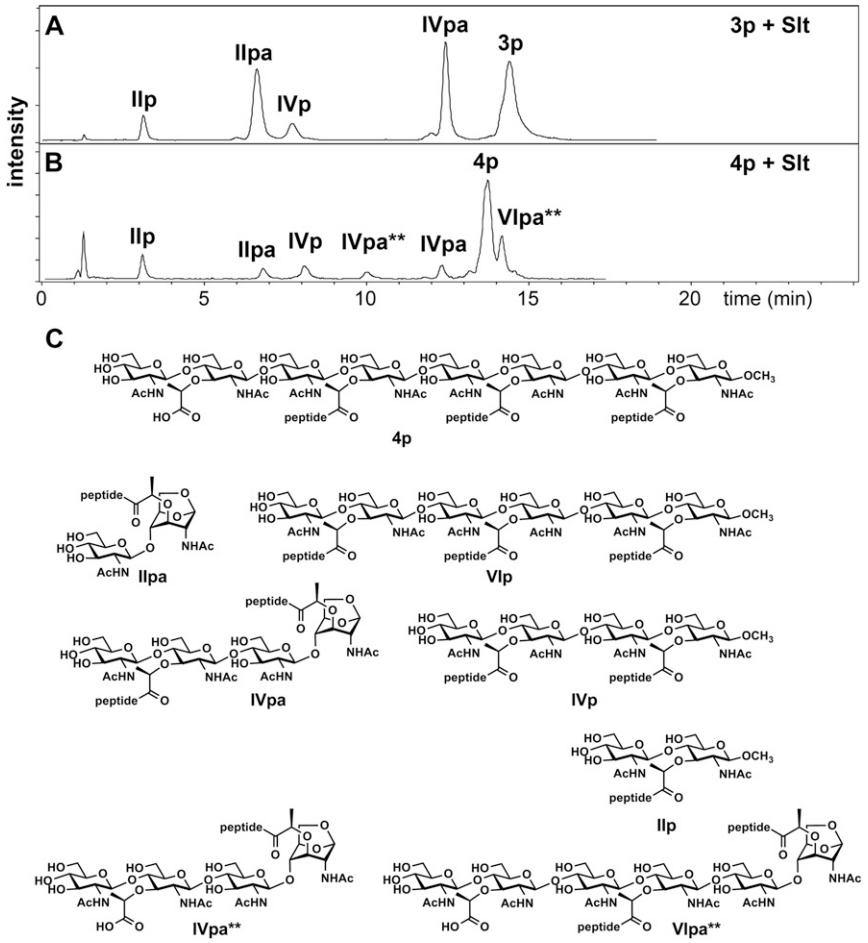

Fig. S2. Turnover of octasaccharides catalyzed by Slt. (*A* and *B*) LC/MS traces of turnover of **3p** and **4p** catalyzed by Slt. (*C*) The chemical structures of **4p** and possible turnover products of **4p**. The position of the missing peptide can be the first, second, or third NAM from the left side of molecule (1). **IVpa**** and **VIpa**** have one less pentapeptide than **IVpa** and **VIpa**, respectively. The given structures are examples of two and three possible structures of **IVpa**** and **VIpa****. The position of missing peptide was not determined. Slt prefers substrate containing the peptide stems, but it also can turnover substrate such **4p**.

1. Lee M, et al. (2017) Deciphering the nature of enzymatic modifications of bacterial cell walls. *Chembiochem* 18:1696–1702.

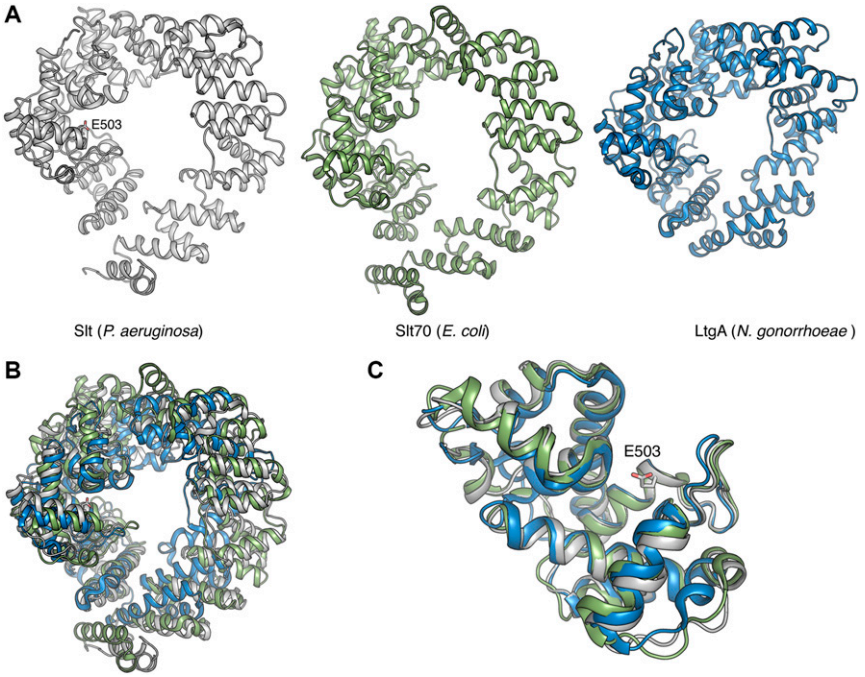

Fig. S3. (*A*) Three-dimensional structures of Slt from *P. aeruginosa* (this work; gray ribbon) and its closest homologs Slt70 from *Escherichia coli* (PDB ID code 1QSA; green ribbon) and LtgA from *Neisseria gonorrhoeae* (PDB ID code 5MPQ; blue ribbon) are depicted. The side chain of the catalytic residue Glu503 is labeled and showed as capped sticks. (*B*) Superimposition of Slt with Slt70 and with LtgA. Main differences are found in the U and L domains, whereas the C-terminal domains are highly conserved. (*C*) Structural superimposition of the C-terminal domains (catalytic domains) of Slt, Slt70, and LtgA shows high similarity (rmsd of 0.6 and 1.1 Å for Slt70 and LtgA, respectively).

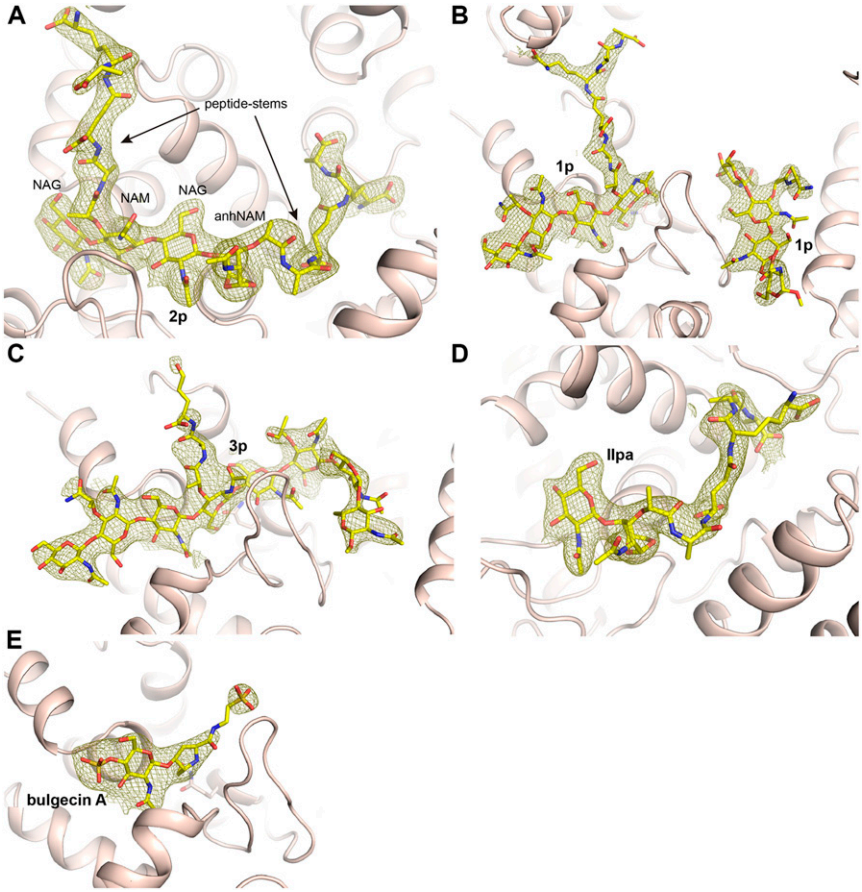

Fig. S4. Electron density maps for the Slt complexes. (*A*) Electron density map (2Fo-Fc map contoured at 1σ) for the Slt:**2p** complex. The ligand occupies subsites −2 to +2. (*B*) Electron density map (2Fo-Fc map contoured at 1σ) for two molecules of **1p** bound to the active site (the Slt:**1p** complex). Ligands occupy subsites −4 to −1 and +3 to +6. The electron density is complete for the peptide stem at subsite −1, but partial for the other peptide stems. (*C*) Electron density map (2Fo-Fc map contoured at 0.8σ) for the Slt:**3p** complex. The ligand occupies subsites −4 to +4. Electron densities for peptide stems were not observed, except for a partial one at subsite −1. (*D*) Electron density map (2Fo-Fc map contoured at 1σ) for compound **llpa** (Slt:**llpa** complex) bound at subsites +1 and +2. (*E*) Electron density map (2Fo-Fc map contoured at 1σ) for bulgecin A bound at subsites −3 to −1.

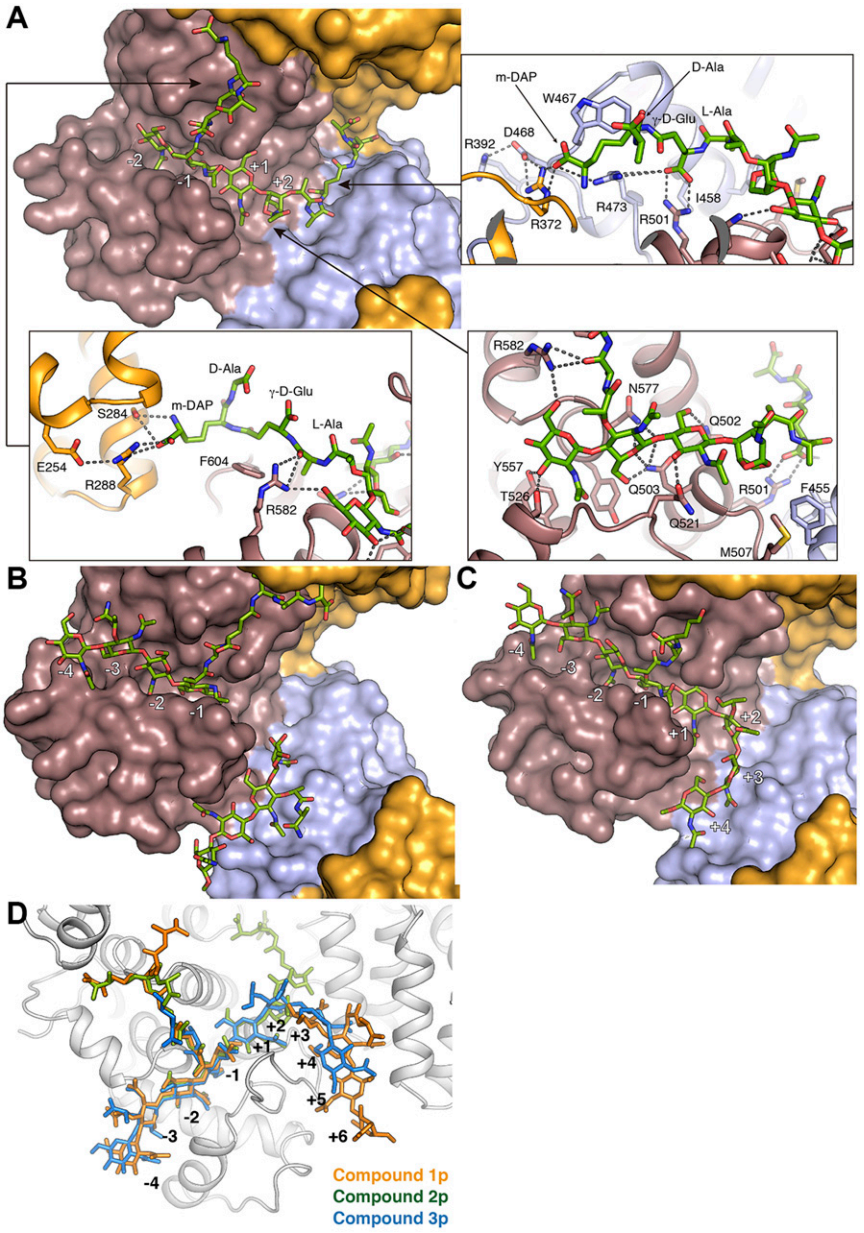

Fig. S5. Interaction of the different peptidoglycan substrates analyzed in this work onto the binding sites of Slt. The enzyme is represented by its Connolly surface and colored by domains (C in brown, U in orange, and L in blue), and compounds are represented as capped sticks. (*A*) Crystal structure of the Slt:**2p** complex. The binding subsites are labeled. Details of the interactions stabilizing both the peptide stems at −1 and +2 sites, and the glycan chain are shown as separate panels. (*B*) Crystal structure of the Slt:**1p** complex. Two molecules of **1p** are found attached to Slt, one of them at the active site (positions are labeled) and the second one, bound to the secondary binding site formed at the interface of the catalytic and the L domains. (*C*) Crystal structure of the Slt:**3p** complex. The octasaccharide is bent interacting with the active and secondary/endolytic sites. (*D*) Structure of the Slt:**3p** complex (protein depicted as gray ribbons) with the compound **3p** represented as blue sticks. Compounds **1p** (orange sticks) and **2p** (green sticks), as observed in Slt:**1p** and Slt:**2p**, respectively, are superimposed.

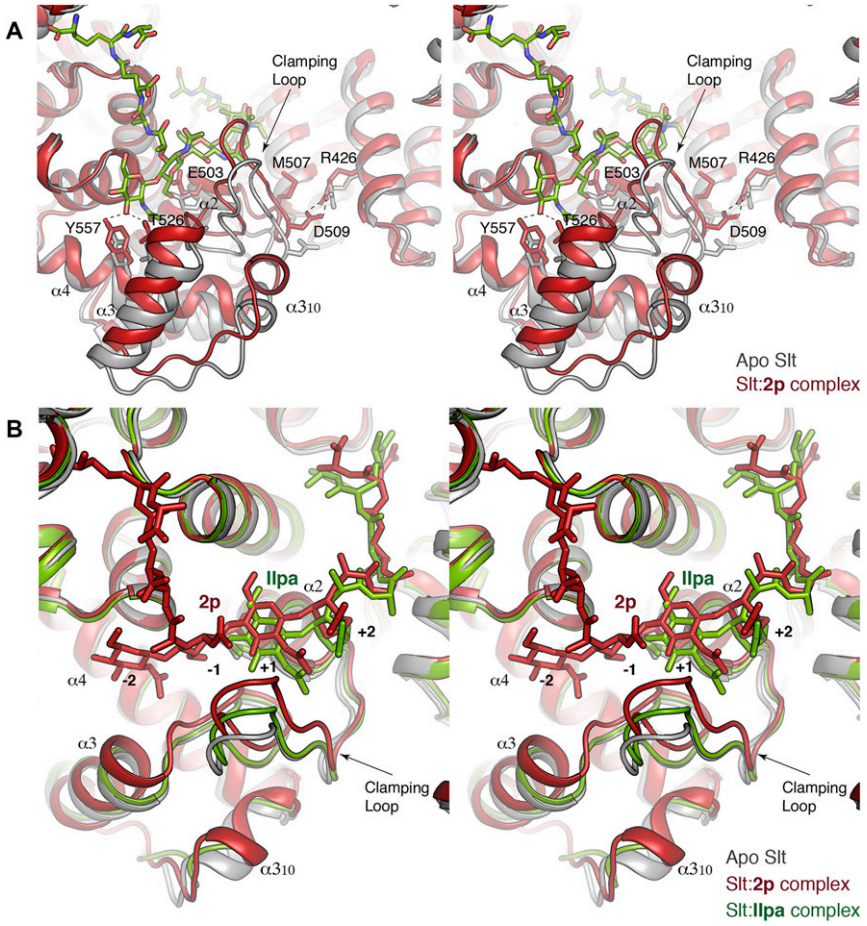

Fig. S6. Activation mechanism and product release for exolytic activity of Slt. (*A*) Stereoview of the comparison of the apo Slt and the Slt:**2p** complex. The apo Slt structure (gray ribbon) and Slt:**2p** complex structure (red ribbon), with the compound **2p** shown as capped sticks (colored in green for the C atoms). Changes occur mainly on one lobe of the catalytic domain (the involved helices and residues are labeled). New interactions between Y557, T526, and NAG, and between D509 and R496 are showed in dashed lines. These interactions are likely involved in promotion of catalysis. (*B*) Stereoview showing the superposition of the apo Slt (gray), the complex with the exolytic substrate (Slt:**2p** complex, red), and the complex with the reaction product (Slt:**IIpa** complex, green). Interaction with the substrate triggers activation by movement of a lobe of the catalytic domain (comprising α-helices 2–4, helix 3_{10}, and the clamping loop; see *B* for details); upon catalysis, the clamping loop retracts toward the apo position, widening the active site and promoting movement of the substrate at positions +1 and +2.

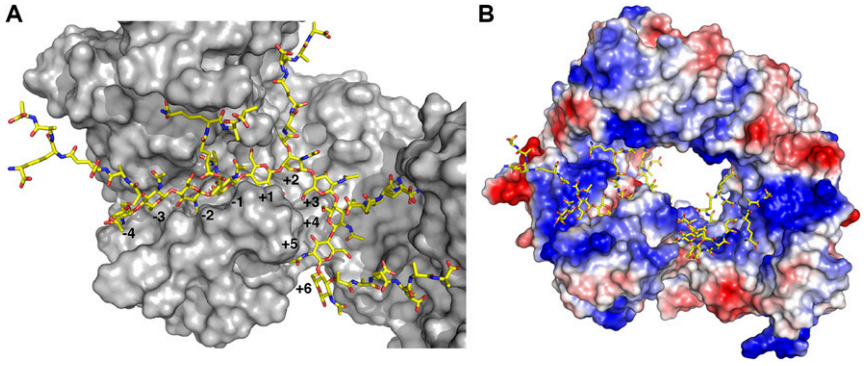

Fig. S7. (*A*) Computational model of peptidoglycan (yellow carbon), obtained from the crystal structures of Slt:**1p** and Slt:**3p** complexes, bound to the active site of Slt enzyme (gray surface) with occupancy on subsites −4 to +6. The image was rendered after clipping the viewing plane. (*B*) Electrostatic potential surface of Slt in complex with the computational model of peptidoglycan (sticks). On surface, basic patches are shown in blue and acidic patches in red.

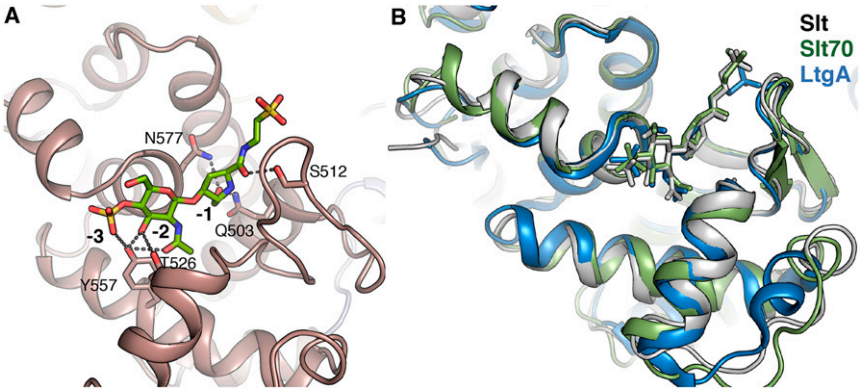

Fig. S8. Bulgecin A inhibition of Slt. (*A*) View of the bulgecin A bound to the active site of Slt as observed in the Slt:bulgecin A complex. The catalytic subsites are labeled, and the inhibitor is shown as capped sticks in green for the carbon atoms. Residues interacting with the inhibitor are depicted as capped sticks and labeled. (*B*) Overall structural superimposition of Slt:bulgecin A complex (gray ribbon) (this work), Slt70:bulgecin A complex (green ribbon) (PDB ID code 1SLY), and LtgA:bulgecin A complex (blue ribbon) (PDB ID code 5MPQ). Bulgecin A is represented as capped sticks.

Table S1. Crystallographic data

Parameter	Slt	Slt E503Q	Slt:**1p** complex	Slt:**2p** complex	Slt:**3p** complex	Slt:**IIpa** complex	Slt:bulgecin A complex
Data collection statistics							
Wavelength, Å	1.0000	0.97953	0.97926	0.97926	0.97953	0.97919	0.97953
Space group	P 6_3	P 6_3	P 6_3	P 6_3	P 6_3	P 6_3	P 6_3
a, *b*, *c*, Å	163.98,163.98,56.71	163.48,163.48,56.04	166.87,166.87,54.51	166.70,166.70,55.34	164.29,164.29,55.95	165.52,165.52,54.73	165.71,165.71,55.88
α, β, γ, °	90,90,120	90,90,120	90,90,120	90,90,120	90,90,120	90,90,120	90,90,120
Resolution range, Å	47.34–2.20 (2.28–2.20)	47.19–3.05 (3.16–3.05)	48.17–2.90 (3.00–2.90)	48.12–2.75 (2.85–2.75)	47.43–3.20 (3.32–3.20)	47.78–2.50 (2.59–2.50)	46.33–3.10 (3.21–3.10)
Unique reflections	44,559 (3,846)	16,595 (1,642)	19,575 (1,939)	23,200 (2,285)	14,530 (1,445)	30,002 (2,985)	15,755 (1,566)
Completeness, %	99.98 (100.0)	99.88 (99.94)	99.92 (100.0)	99.92 (99.91)	99.91 (100.0)	99.93 (100.0)	97.11 (98.99)
Multiplicity	19.4 (19.3)	11.7 (2.4)	9.9 (0.9)	9.7 (1.2)	9.4 (1.3)	15.2 (1.8)	16.5 (1.9)
CC1/2	0.99 (0.72)	0.99 (0.66)	0.99 (0.31)	0.99 (0.65)	0.99 (0.68)	0.99 (0.74)	0.99 (0.79)
R_{pim}	0.05 (0.86)	0.048 (0.39)	0.092 (1.00)	0.052 (0.53)	0.061 (0.48)	0.024 (0.36)	0.037 (0.37)
Average $I/\sigma(I)$	14.8(1.35)	11.94 (2.09)	9.91 (0.88)	9.65 (1.22)	9.35 (1.29)	15.2 (1.8)	16.53 (1.93)
Refinement statistics							
Resolution range, Å	47.34–2.20	47.19–3.05	48.17–2.90	48.12–2.75	47.43–3.20	47.78–2.50	46.33–3.10
R_{work}/R_{free}	0.18/0.24	0.19/0.25	0.21/0.27	0.20/0.24	0.20/0.27	0.18/0.24	0.20/0.22
No. atoms							
Protein	5,010	5,006	4,977	4,977	4,972	4,978	4,986
Water	363	71	57	131	57	96	76
Ligand	40	6	180	138	149	94	41
Root-mean-square deviations							
Bond length, Å	0.007	0.008	0.009	0.009	0.009	0.013	0.008
Bond angles, °	0.877	1.23	1.37	1.28	1.34	1.61	1.25
Ramachandran favored/outliers, %	99.4/0.6	96.1/0.2	97.0/0.5	97.6/0.0	93.6/0.3	96.4/0.3	96.4/0.3
Residues in the AU	613	614	613	613	613	610	613
PDB ID code	5OHU	6FC4	6FCS	6FCR	6FCU	6FBT	6FCQ

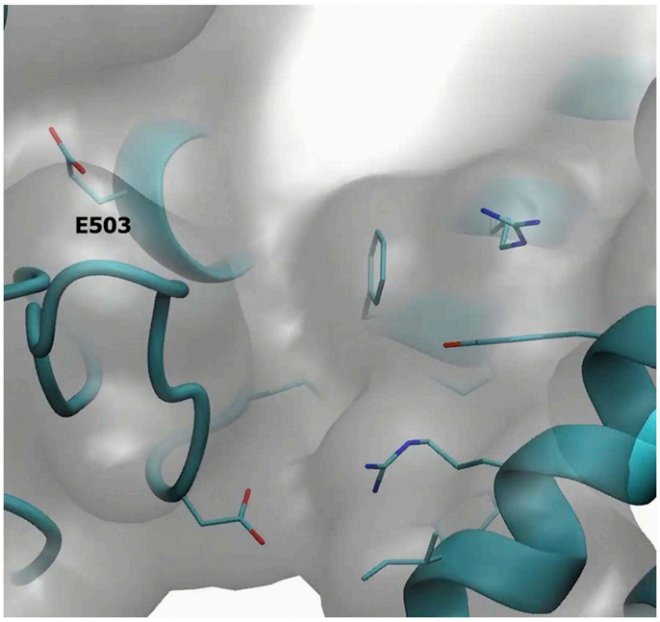

Movie S1. Morph animation of the reorganization of the active site for endolytic reaction. The motion was morphed from the apo X-ray structure toward the Slt:**3p** complex.

Movie S1

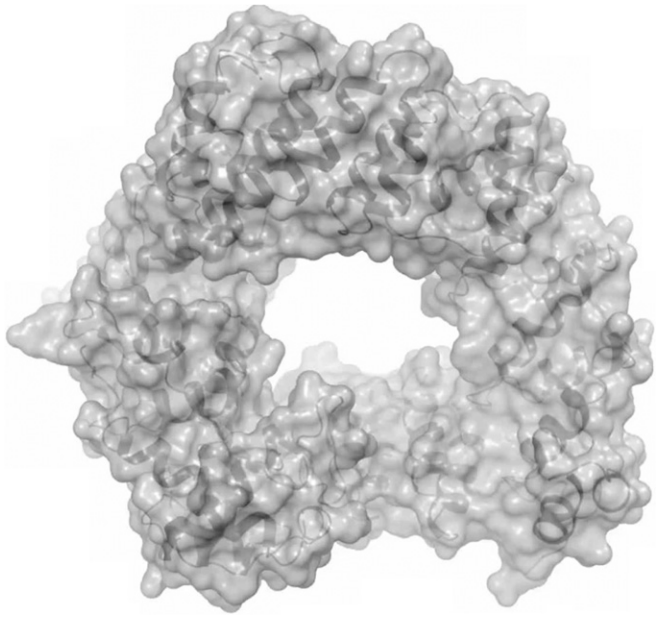

Movie S2. Morph animation of the conformational motion experienced by the entire protein. The motion was morphed from the apo X-ray structure toward the Slt:**3p** complex.

Movie S2